ROYAL SOCIETY OF CHEMISTRY

PAPER

Check for updates

A self-assembled three-dimensional hierarchical nanoflower: an efficient enzyme-mimetic material for cancer cell detection that improves ROS generation for therapy†

Chandran Murugan, [ID] Hyoryong Lee and Sukho Park [ID] *

Three-dimensional (3D) nanomaterials with high functional properties are emerging as the most promising artificial enzymes for overcoming the significant disadvantages of natural enzymes. Anticancer therapy using 3D-enzyme mimetic materials has emerged as an essential development for catalyzing cancer cell destruction. We report for the first time a novel 3D-based enzyme mimetic material, $CaMoO_4/MoS_2/CuS$ nanoflower (CMC NF), that exhibits a large specific surface area, uniform flower-like structure, excellent biocompatibility, and high porosity, making it a suitable candidate for cancer detection and therapy. Additionally, CMC NFs were conjugated with folic acid (FA) to selectively target cancer cells, resulting in FA–CMC NFs explicitly binding to overexpressed folate receptor alpha (FRα) in MDA-MB-231 cells. Based on the peroxidase activity, the FA–CMC NFs are an effective nanoprobe for the selective detection of MDA-MB-231 cells over a wide detection range (50 to 5.5×10^4 cells per mL) with a low limit of detection (LOD) value of 10 cells per mL. In addition to their cancer detection capability, the FA–CMC NFs also effectively generated $^{\cdot}OH$ radicals in a concentration-dependent manner to treat cancer cells. Under light conditions, the FA–CMC NFs with H_2O_2 solution showed efficient degradation of methylene blue (MB) dye, and the solution color appeared to fade within 15 min, indicating that they generated $^{\cdot}OH$ radicals, which can efficiently kill cancer cells. Thus, the superior functionality of FA–CMC NFs offers cost-effective, facile, and reliable cancer cell detection, providing a new treatment option for cancer treatment and diagnosis.

1 Introduction

An innovative anticancer therapy based on nanozymes has gained significance, inspired by the enzymes found in natural defenses that catalyze the destruction of cancer cells.[1,2] Nanozymes are nanomaterials that possess enzyme-like activities intrinsically and have been widely used in biomedicine for years.[3–5] In recent years, there has been increased interest in developing nanozymes to catalyze biological reactions that can aid in cancer detection and therapy, among other applications.[6,7] Nanozymes can imitate the functions of peroxidase (POD) and oxidase (OXD) and produce ROS, which is toxic to cancer cells in large amounts.[8] Many naturally occurring enzymes contain metal catalytic centers primarily composed of Fe, Cu, Mn, or Zn ions. For example, many proteins and enzyme catalytic centers are made of copper.[9,10] The copper-based nanozyme holds several benefits, such as a lower redox

potential for Cu^{2+} to Cu^+, which results in a higher reaction rate with H_2O_2 than Fe^{2+}, indicating that Cu^+ displays more peroxide-like activities than Fe^{2+}.[11,12] Copper-based nanoparticles are valued for their Fenton-like activity and are utilized as a potent and effective antitumor agent. However, to enhance the selectivity and efficacy of cancer treatment in the tumor microenvironment, reductive agents like GSH can convert Cu^{2+} to Cu^+ species. Unfortunately, prior research has demonstrated that using CuNPs can lead to hepatotoxicity, nephrotoxicity, and severe injury in mice and rats[13,14] and induce gill toxicity in zebrafish.[15] Expanding the research on Cu-based nanozymes may be facilitated by creating new copper-based candidates that exhibit biological or biocompatible properties; however this remains a difficult task. Furthermore, for practical purposes, typical peroxidase systems may be replaced by new generation Cu-based hybrid nanostructures with peroxidase-mimetic activity.

In other words, one of the most intriguing materials is calcium molybdate ($CaMoO_4$) nanoflowers because of their scheelite structure and superior chemical and physical properties, such as a wide band gap (3.6 eV), high absorption cross-section (~103 cm^{-1}), and high melting point (1445–1480 °C) as

Department of Robotics and Mechatronics Engineering, Daegu Gyeongbuk Institute of Science and Technology (DGIST), Daegu 42988, Republic of Korea. E-mail: shpark12@dgist.ac.kr

shown in ref. 16 and 17. The CaMoO$_4$ crystal structure includes tetrahedrally coordinated anionic [MoO$_4$]$^{2-}$ groups and cationic Ca^{2+} groups that bond with eight oxygen atoms, forming an octahedron structure and leading to a more stable complex system of CaMoO$_4$.[18] Combining CaMoO$_4$ with Fe$_3$O$_4$–Eu metal nanoparticles had no significant dose-dependent toxic effects on mesenchymal stem cells (hTERT cells), even at higher concentrations.[19] As a result, creating nanozymes with copper and CaMoO$_4$ could improve biocompatibility and enhance analytical capabilities, making it easier to detect and treat breast cancer cells.

Herein, we have developed a new 3D nanoflower composed of CaMoO$_4$/MoS$_2$/CuS that exhibits peroxidase-mimetic activity for the *in vitro* detection and therapy of breast cancer cells. The nanoflowers were created through a cost-effective hydrothermal method, which involved heating precursor solutions at 180 °C. To target cancer cells specifically, the nanoflowers were subsequently conjugated with folic acid using a (N-hydroxysuccinimide selectively)/N-ethyl-N′-(3-(dimethylamino)propyl) carbodiimide (NHS/EDC) coupling agent. The obtained CMC NFs showed unexpected peroxidase-like activity when they catalytically oxidized the TMB substrate in the presence of H$_2$O$_2$. Due to their exceptional peroxidase mimetic activity, FA–CMC NFs were utilized for quantitative cancer cell detection. When they were combined with methylene blue (MB) under light (1 W LED) conditions, the NFs generated reactive oxygen species (˙OH radicals) that drastically killed the effect on cancer cells. Therefore, the CMC NFs provide an efficient and sensitive approach for detecting cancer cells and will have more widespread applications in early disease diagnosis and therapy.

2 Results and discussion

Three-dimensional (3D) calcium molybdate–copper molybdenum sulfide nanoflowers (CMC NFs) were formed through hydrothermal synthesis using calcium molybdate (CaMoO$_4$) forming components (CaCl$_2$, Na$_2$MoO$_4$·2H$_2$O, and PVP) with MoS$_2$/CuS producing components (CH$_4$N$_2$S, C$_6$H$_8$O$_7$, and CuH$_2$N$_2$O$_7$), respectively. The formation of the nanoflowers was carried out in an aqueous solution, with the possible mechanism being the reaction between calcium chloride and sodium molybdate, resulting in the formation of the prominent CaMoO$_4$ material in the CMC NFs. The PVP was used to control the nanoflowers' morphology and stabilize their surface.

$$CaCl_2 + Na_2MoO_4 \rightarrow CaMoO_4 + 2NaCl$$
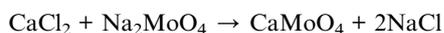
Then, at a higher temperature (180 °C), the sulphur (S) ions react with excess MoO$^-$ ions and subsequently interact with Cu^{2+} ions reduced from CuH$_2$N$_2$O$_7$ in the presence of citric acid (CA); this leads to the formation of MoS$_2$/CuS. The developed components are then self-assembled into CMC NFs at 180 °C. The synthesized CMC NFs were refluxed with 3-APTES to obtain –NH$_2$ functionalized CMC NFs (3-APTES/CMC NFs). Then, FA was conjugated onto 3-APTES/CMC NFs through a coupling reaction between –NH$_2$ and FA-activated ester using NHS/EDC,

attaining FA–3-APTES/CMC NFs. Finally, the desired FA–CMC NFs were applied to detect and treat cancer cells. The overall synthetic strategy and applications of 3D-CMC NFs are illustrated in Fig. 1.

The morphology and structure of the synthesized CMC NFs were analyzed using TEM and SEM, respectively. As illustrated in Fig. 2A, SEM images confirmed the presence of uniform hierarchical 3D-flower-like spherical structures, good dispersion, high porosity, and a high surface-to-volume ratio. High-resolution FE-SEM images in Fig. 2B and C show the CMC NFs with manifold thin petals and abundant porous structures with closely interlaced petals, consistent with previous reports.[20,21] The low magnification TEM image revealed that the nanoflower had a unique 3D hierarchical morphology, with an average size above 500 nm, exhibiting excellent dispersion without significant aggregation and uniform flower-like structures, as shown in Fig. 2D. The HR-TEM images displayed the CMC NF petals, which consisted of well-stacked interlayer lattice fringes, petal-like designs on the surface, and distribution of micro/mesopores, as shown in Fig. 2E and F. As observed in HR-TEM (Fig. 2G), the lattice fringe spacing was 0.19 nm, nearly the same as the d' value of the hexagonal CuS (110) plane.[22] Furthermore, the d' value of the (001) facets of MoS$_2$, which was nearly equal to the lattice fringes of 0.27 nm, and the line profile for its inverse fast Fourier transform (FFT) confirmed the presence of a crystalline structure in the CMC NFs as shown in Fig. 2H and S1 (ESI†).[23] As shown in Fig. 2I, selected area electron diffraction (SAED) showed that the concentric rings had many bright spots, and the diffraction peaks at (101), (112), (004), (200), (114), (204), (220), (116), and (215) planes (red arrows) corresponded to CaMoO$_4$.[24] Notably, five diffraction rings with strong reflections (white arrows), such as (100), (102), (110), (220) and (300) planes, corresponded to CuS.[25] In addition, the SAED pattern of CMC NFs consisted of a series of diffraction peaks associated with CuS and CaMoO$_4$ structures, respectively. The analysis revealed that the 3D-CMC NFs consist of a predominant amount of CaMoO$_4$ and a smaller amount of MoS$_2$/CuS based on the formation.

The energy dispersive X-ray (EDX) elemental mapping showed a homogeneous distribution of copper (Cu), molybdenum (Mo), sulphur (S), calcium (Ca), and oxygen (O) elements in the prepared CMC NFs (Fig. 3A). The quantitative EDX data showed that the percentage of elements in the CMC NFs was calculated to be 36.3% Cu, 20.05% Mo, 28.7% S, 13.03% O, and 1.91% Ca, respectively, which further confirmed the formation of CaMoO$_4$, MoS$_2$, and CuS in the CMC NFs (Fig. S2, ESI†). To confirm the phase purity of CMC NFs, the X-ray diffraction (XRD) pattern was recorded (Fig. 3B). The results revealed that the peaks matched well with the standards CaMoO$_4$ (JC PDS no. 01-077-2238), MoS$_2$ (JCPDS card no. 37-1492) and CuS (JCPDS card no. 01-078-0877), indicating the successful synthesis of CMC NFs. No peaks of other impurity phases were detected in the patterns, suggesting that hydrothermal synthesis can easily attain NFs with high phase purity. The diffraction peaks were detected at 2θ = 18.668°, 28.765°, 31.292°, 34.318°, 39.870°, 47.12°, 49.319°, 54.15°, 56.281°, and 58.09°, which correspond to the (101), (112), (004), (200), (114), (204), (220), (116), (125),
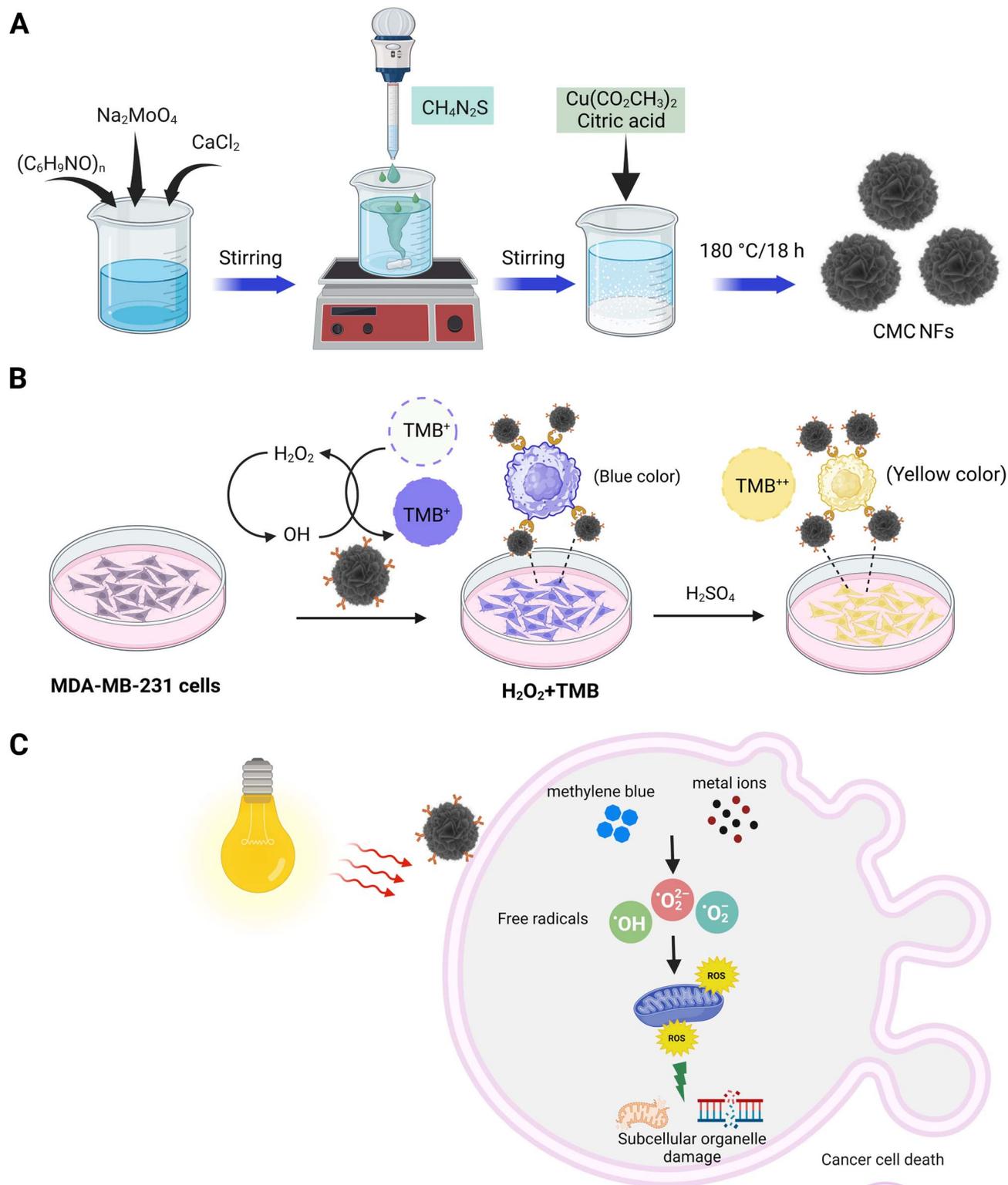
Fig. 1 Schematic depiction of (A) the proposed reaction for the fabrication of CMC NFs by a simple hydrothermal approach at 180 °C. (B) The overall surface modification procedure of the synthesized NFs to achieve FA-conjugated CMC NFs that bind obviously with MDA-MB-231 cells *via* overexpressed folate receptor alpha. (C) Schematic illustration of the peroxidase activity of CMC NFs in the presence of TMB and H_2O_2, which were used for cancer cell detection, as well as the treatment efficacy of CMC NFs with methylene blue (MB) dye towards MDA-MB-231 cells under 1 W LED light conditions.
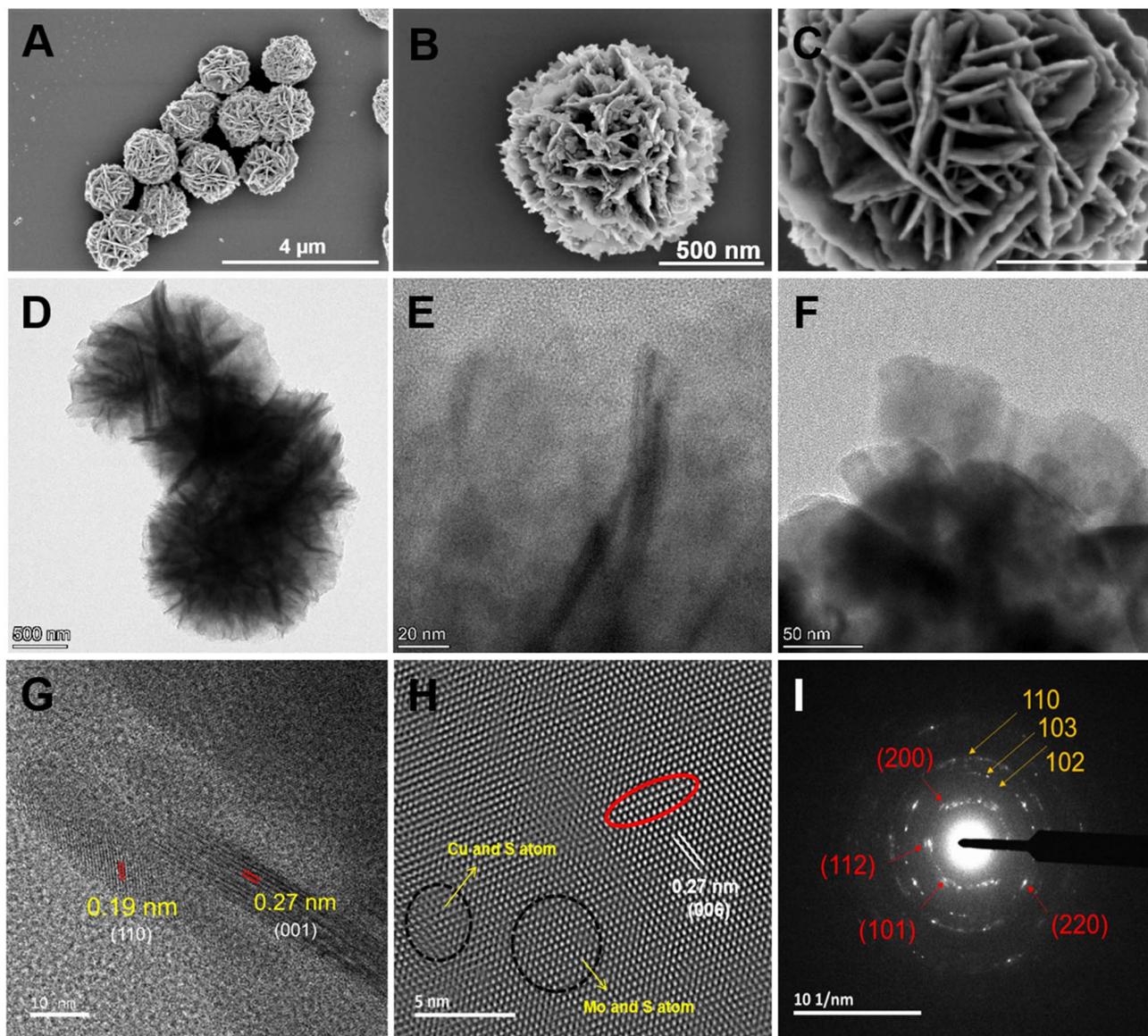
Fig. 2 Morphology and structural characterization of 3D-CMC NFs. (A–C) Low and high-resolution SEM images illustrating the assembly of the 3D-CMC NFs from ultra-thin nanosheets, exhibiting a flower-like morphology and porous structure, (D) TEM image showing a unique 3D hierarchical morphology with a flower-like structure, (E) the higher-resolution TEM (HR-TEM) image depicting the lattice fringe and (F) petal-like designs on the nanoflower surface, and (G and H) HR-TEM images depicting the lattice spacings in different crystalline domains, and (I) SAED pattern of CMC NFs.

and (312) crystal planes of $CaMoO_4$, respectively, and the result was consistent with a previous report.[24] The 2θ of 32.7° and 58.5° of hexagonal MoS_2 corresponds to the (100) and (110) crystal planes, which could be well indexed to the standard XRD pattern.[26] The diffracted peaks of CuS at 2θ values of 27.7°, 29.2°, 32.3°, 48.3° and 53.8° correspond to the (101), (102), (103), (110), and (108) crystal planes, respectively.[27] The results suggest that the hydrothermal method improved the crystal structure of the as-prepared CMC NFs. The EDX spectrum analysis revealed that the CMC NFs are a mixture of $CaMoO_4$, MoS_2, and CuS nanostructures. The SAED pattern displayed a combination of rings and dots, indicating the presence of mixed polycrystalline metal oxides in the CMC NFs.

To investigate the intrinsic structure and surface conditions of CMC NFs, Raman spectroscopy was performed within the range of 0–1200 cm^{-1} (Fig. 3C). The result revealed eight vibrational modes attributed to the identical motion behavior of the clusters in the $CaMoO_4$ lattice and the vibration mode of MoS_2/CuS. These modes were assigned to the stretching vibrations of Mo–S, Cu–S, and S–S. An intense mode at 879 cm^{-1} of $CaMoO_4$ indicated symmetric Mo–O stretching vibrations, which were allocated to $\nu_{s(1)}(A_g)$ (Mo–O). Furthermore, a peak at 847 cm^{-1} confirmed the antisymmetric stretching mode, which corresponded to $\nu_{as(3)}(B_g)$ (Mo–O). Additionally, other modes, including $\nu_3(E_g)$, $\nu_4(E_g)$, and $\nu_4(B_g)$ of $CaMoO_4$, were observed at 794, 389, and 323 cm^{-1}, respectively. The observed external and
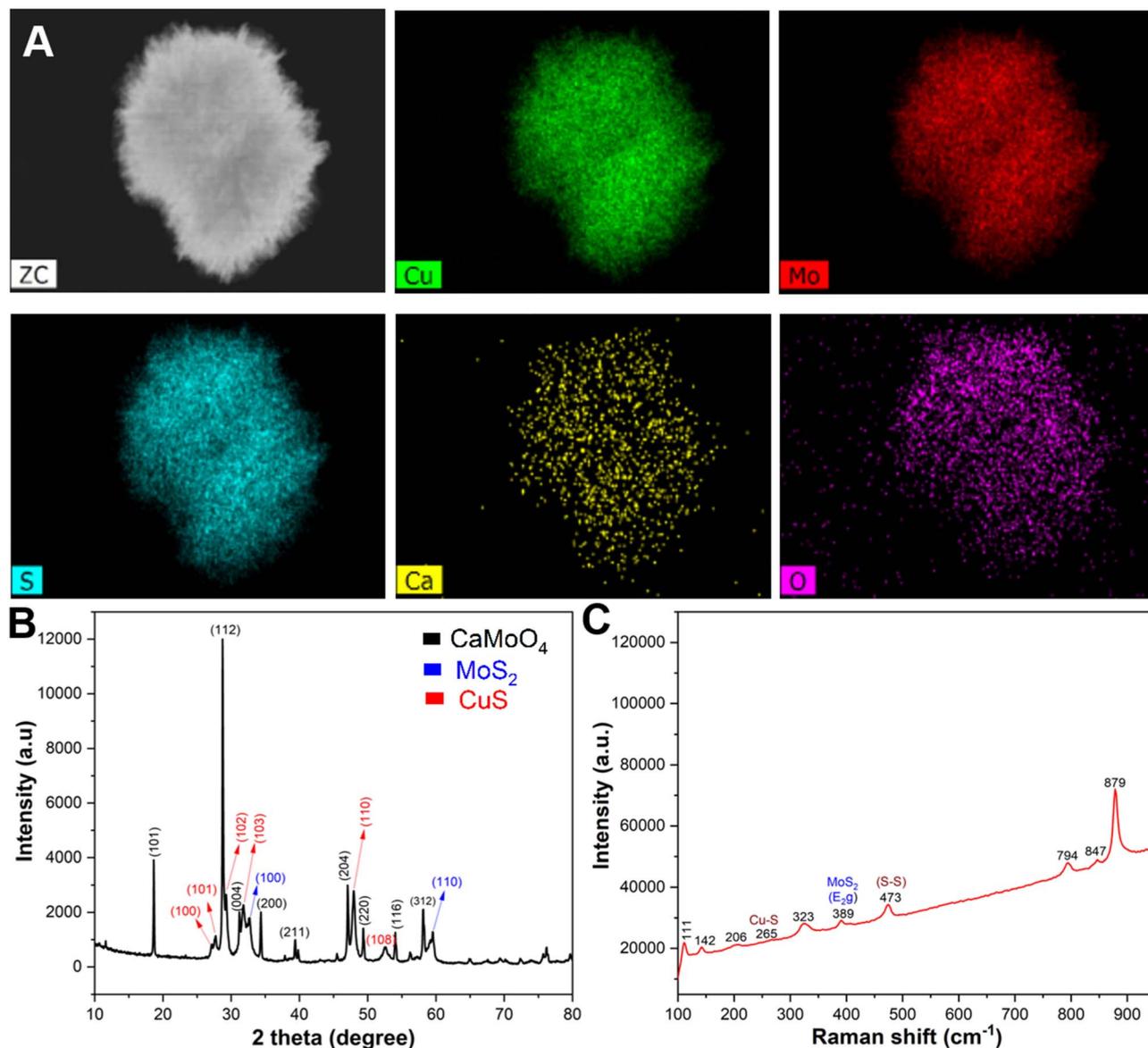
Fig. 3 (A) Elemental mapping of Cu, Mo, S, Ca, and O corresponding to the as-prepared NFs acquired by the energy dispersive X-ray (EDX) analysis. (B) XRD pattern of CMC NFs and it matched with that of $CaMoO_4$ (JC PDS no. 01-077-2238), MoS_2 (JCPDS card no. 37-1492) and CuS (JCPDS card no. 01-078-0877), and (C) Raman spectra recorded to investigate the surface oxidation states and chemical composition of CMC NFs in the range of 0–1200 cm^{-1}.

internal $CaMoO_4$ modes result from the lattice vibrations of Mo^{2+} metal ions and the rigid $[MoO_4]^{2-}$ units and vibrations within the $[MoO_4]^{2-}$ molecular units, respectively.[24] A characteristic band at 385 cm^{-1} confirms the presence of the E_{2g} band of MoS_2 due to in-plane vibrations. A band at 473 cm^{-1} is attributed to the S–S lattice stretching vibration of CuS, while the small band at 265 cm^{-1} is assigned to the Cu–S vibrational mode.[28] The infrared active peaks at 111 and 142 cm^{-1} are due to the defects of Cu_2O.[29]

X-ray photoelectron spectrum (XPS) measurement was performed to analyze the surface oxidation and chemical composition states of CMC NFs (Fig. 4). The XPS survey spectrum of the CMC NFs covered the 0–1200 eV binding energy range, and the peaks indicated the presence of Cu 2p, Mo 3d, S 2s, Ca 2p, O

1s, and C 1s states. The binding energy at 931.2 and 951.3 eV was assigned to the Cu $2p_{3/2}$ and Cu $2p_{1/2}$ states, which were attributed to the Cu(I) and Cu(II) sites.[30] In the Mo 3d spectrum, two prominent peaks at 229.8 and 232.9 eV were assigned to Mo $3d_{5/2}$ and Mo $3d_{3/2}$, respectively. The 3.11 eV energy difference between these Mo 3d peaks confirmed the presence of the Mo^{6+} state in molybdenum oxides. Additionally, a small peak confirmed the S 2s state at 226.5 eV, and the presence of two prominent characteristic peaks of the S 2p spectrum at 162.4 and 163.5 eV can be attributed to S $2p_{3/2}$ and S $2p_{1/2}$ states indicating the domain oxidation state of S^{2-}.[31] Two peaks at 351.2 and 346.5 eV were observed in the Ca 2p spectrum and were assigned to Ca $2p_{1/2}$ and Ca $2p_{3/2}$ in $CaMoO_4$. The gap of 3.4 eV between the Ca 2p peaks confirms the oxidation state of
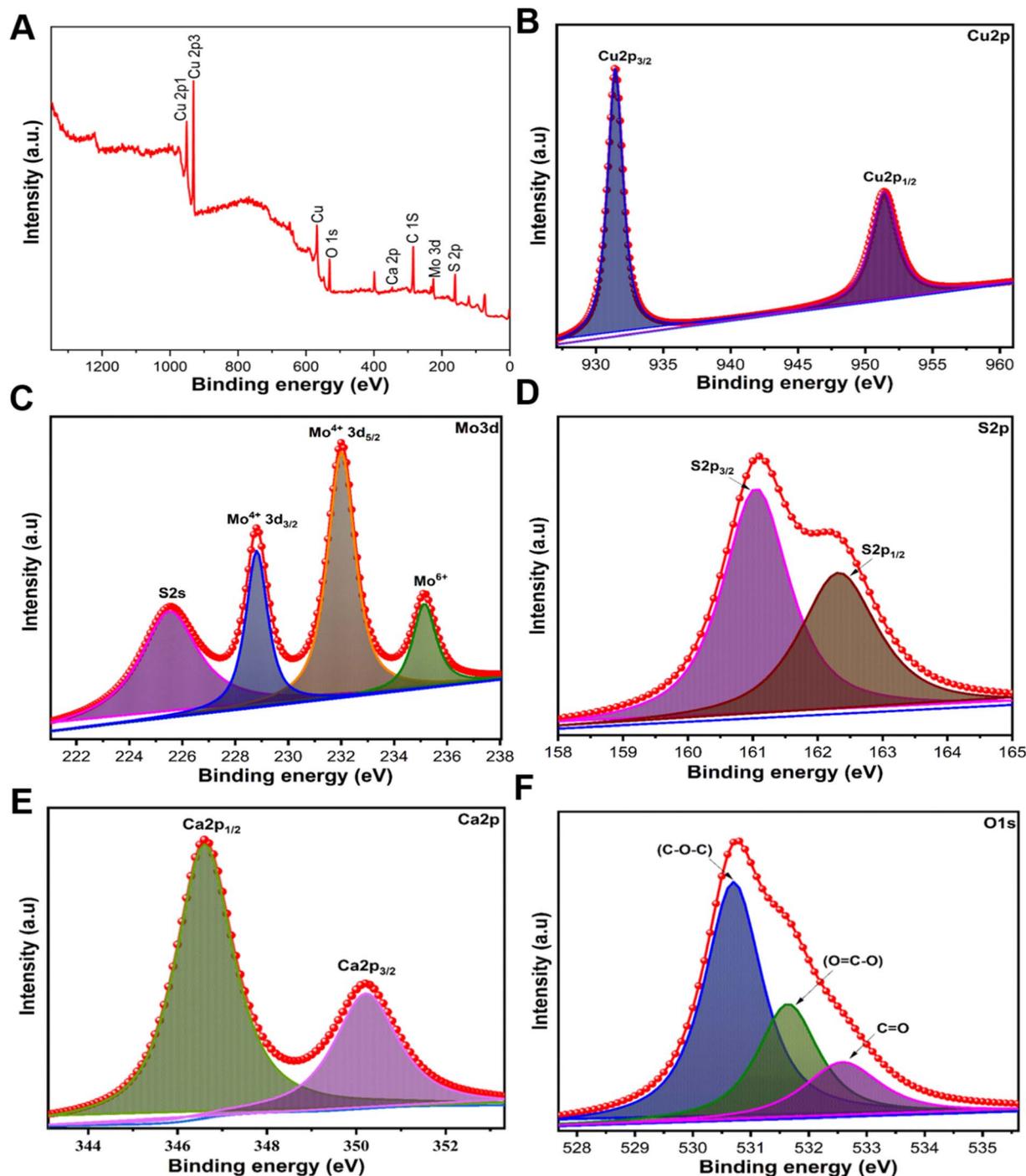
Fig. 4 High-resolution XPS spectra of CMC NFs, spectra for the (A) survey spectrum, (B) Cu 2p spectra, (C) Mo 3d spectra, (D) S 2s spectra, (E) Ca 2p orbit, and (F) O 1s spectra.

Ca^{2+}.[32] In the O 1s spectrum, two peaks at 532.68 and 530.69 eV were observed due to the chemisorbed oxygen and lattice oxygen on the $CaMoO_4$ surface. The C 1s spectrum showed two peaks at 289.5 and 285.0 eV, which were assigned to the C=O and C–C functional groups due to carbon contamination (Fig. S3, ESI†). The appearance of all the peaks confirms the $CaMoO_4$, MoS_2, and CuS formation in CMC NFs.

The CMC NF peroxidase-like activity was examined through catalytic oxidation of TMB in the presence of H_2O_2, and the

absorption spectrum was recorded at 652 nm using a nanodrop spectrophotometer. The control experiment showed that the CMC NFs with TMB in the absence of H_2O_2 had no blue color formation (Fig. 5A), and H_2O_2 with TMB in the absence of CMC NFs showed a faint blue color, signifying a low absorbance peak at 652 nm. These findings demonstrate the essential role of CMC NFs and H_2O_2 in catalytic oxidation reactions. Conversely, the interaction of CMC NFs with TMB in the presence of H_2O_2 resulted in an intense absorption peak at 652 nm, indicative of
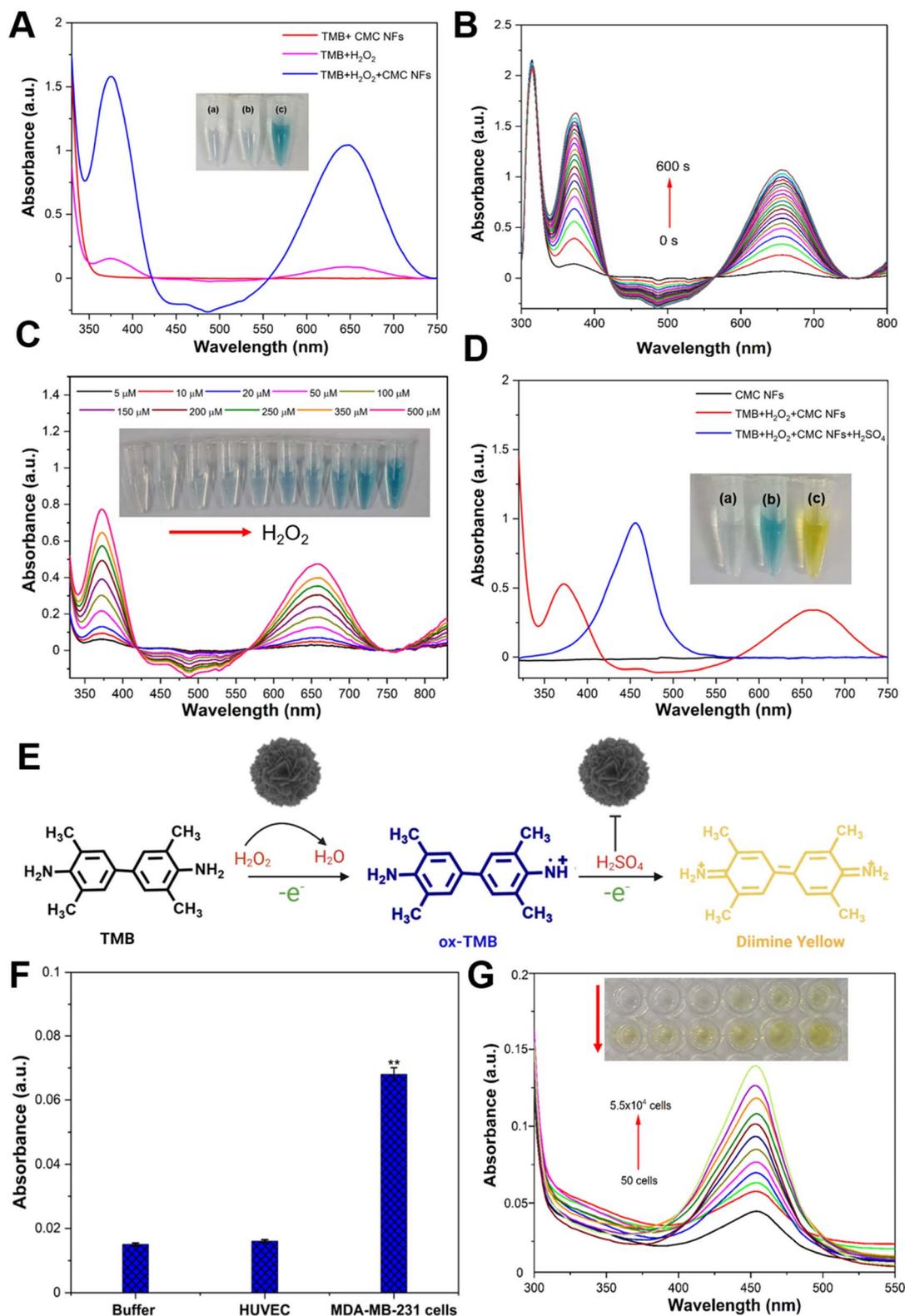
Fig. 5 (A) UV-vis spectra and colour of TMB solution in three catalytic systems; (a) TMB, (b) TMB + H_2O_2, and (c) TMB + H_2O_2 + CMC NFs (blue line) with colour change (inset figure), (B) time-dependent UV-vis absorbance spectrum of the TMB reaction with H_2O_2 catalyzed by CMC NFs, (C) absorbance spectra of TMB oxidation changes with different concentrations of H_2O_2 (5–500 μM), catalysed by CMC NFs and the absorbance spectrum at 652 nm as a function of H_2O_2 concentration, (D) UV-vis absorbance spectra and photographs (from left to right) of TMB oxidation, catalysed by CMC NFs in the presence of H_2O_2 under different conditions: (a) CMC NFs, (b) TMB + H_2O_2 + CMC NFs and (c) TMB + H_2O_2 + CMC NFs + H_2SO_4, (E) schematic illustration of the peroxidase-like performance of the CMC NF nanozyme, (F) target-directed cancer cell detection by FA-conjugated CMC NFs using buffer (control), human umbilical vein endothelial cells (HUVECs) and MDA-MB-231 cells, and (G) selective colorimetric detection of MDA-MB-231 cells in a range from 5×10^1 to 5.5×10^4 cells per mL in the presence of TMB and H_2O_2, catalysed by FA–CMC NFs.

deep blue-colored products and the activity of TMB oxidation by nanoflowers. This activity is similar to that of horseradish peroxidase (HRP) and has been reported to enhance TMB oxidation in the presence of H_2O_2, as previously noted.[33] These findings confirm that CMC NFs exhibit peroxidase-like activity, which can improve TMB oxidation in the presence of H_2O_2. It was also reported that nanoflowers with peroxidase-like activity have the same effect.[34] The K_m value of CMC NFs (0.103 mM) was compared to those of the natural enzyme HRP ($K_m = 0.496$ mM) and other enzyme-mimetic nanomaterials including Au@PNIPAm (0.496 mM),[35] GO–AuNCs (0.16 mM),[36] Fe–N–C SANs (0.13 mM),[37] and $Co(OH)_2/FeOOH/WO_3$ (0.21 mM).[38] K_m is a parameter that measures the affinity between the substrate and enzyme; the result revealed that CMC NFs with a lower K_m value show a higher affinity. This suggests that peroxidase-like CMC NFs have an especially strong affinity for TMB. The literature has previously reported mixed-valence metal oxide or sulfide NPs displaying intrinsic peroxidase-like activity due to Fenton or Fenton-like reactions with H_2O_2. The pH dependence of the catalytic activity of the CMC NFs was investigated using varying pH buffers to optimize the reaction conditions (Fig. S4, ESI†). The results showed that an increase in pH from 2 to 4 led to increased absorbance, while a further increase in pH from 5 to 9 gradually decreased. To assess the enzyme-mimetic activity of CMC NFs under physiological conditions (pH 7.4), the clear absorption of oxTMB and the corresponding blue color indicated relatively lower peroxidase activity of the CMC NFs, as shown in Fig. S5 (ESI†). Acidic pH values played a key role in the peroxidase-like catalytic activity of the CMC NFs. A superior relative catalytic activity was achieved at pH 4, indicating that weakly acidic conditions favor TMB oxidation, and the oxidation rate is reduced under neutral or alkaline pH conditions. Under high pH conditions, the rapid decomposition of H_2O_2 into O_2 leads to insufficient production of $^\bullet OH$ radicals for TMB oxidation. Acidic conditions (pH less than 4) can cause the degradation of the active sites of Cu or Mo, affecting H_2O_2 activation and oxidation of TMB, as reported in previous studies on TMB oxidation; therefore, pH 4 was chosen for further studies. The enzyme-like activity of CMC NFs was investigated using time-dependent absorbance changes at 652 nm in Fig. 5B. As the reaction time increased, the intensity of the absorbance at 652 nm also increased, demonstrating the excellent peroxidase-like activity of CMC NFs. The absorption spectrum of TMB oxidation was analyzed by varying the incubation temperature from 10–70 °C, and it was determined that the maximum absorption occurred at 60 °C. However, the self-decomposition of H_2O_2 at high temperatures resulted in a loss of activity, with only 80% relative activity retention at 70 °C (Fig. S6, ESI†). The ideal temperature and pH for the enzyme-like behavior of CMC NFs were comparable to those of natural enzymes (HPR) and other enzyme mimetic nanomaterials. Therefore, the optimal conditions for the catalytic activity of CMC NFs were determined to be a pH of 4.0, a temperature of 37 °C, and a reaction time of 10 min. The catalytic activity of CMC NFs was studied under these optimal conditions. In a spectrophotometric study conducted at room temperature, the absorbance of TMB at 653 nm increased, similar to the phenomenon observed with

horseradish peroxidase (HRP).[39] These observations suggest that CMC NFs exhibit peroxidase-like efficiency. Bimetallic nanoparticles (BNPs) have enhanced catalytic activity and selectivity compared to monometallic nanoparticles (MNPs) due to the synergistic interaction between two or three different metallic elements combined in one particle.[40] The presence of Cu^{2+} ions on the surface of the CMC NFs may be responsible for the enzyme-like activity, similar to the role of Fe^{3+} in the Fenton-like reaction.[41] The formation of Mo^{6+} ions in MoS_2 also contributes to the decomposition of H_2O_2, resulting in a colored reaction product. Previous studies have shown that Cu-decorated MoS_2 nanosheets have higher catalytic activity against biomolecules in alkaline environments.[42] This observation suggests that the two components' synergistic effect improves the CMC NFs' catalytic activity.

The detection of H_2O_2 is of utmost importance for maintaining human health because it indicates reactive oxygen species (ROS). As part of an experiment aimed at quantifying H_2O_2, various concentrations (5–500 μM) of H_2O_2 were added to CMC NFs and TMB in a buffer solution (pH = 4.0), and the detection was carried out under optimal conditions; the absorbance of the reaction at 652 nm increases as the H_2O_2 concentration increases. The color change in the solution can be easily observed with the naked eye, indicating that CMC NFs are highly sensitive to H_2O_2 analysis (Fig. 5C). The absorbance intensities for various H_2O_2 concentrations were plotted to obtain the reaction's limit of detection (LOD) value (Fig. S7, ESI†). The well-detectable range of H_2O_2 was noted from 1×10^{-4} to 5×10^{-5} mol L^{-1} ($R^2 = 0.99$), and the obtained linear curve of CMC NFs is comparable with those in previous reports.[43,44] The concentration of H_2O_2 was 6 mM, the TMB concentration was varied from 0.05 to 5.0 mM and the K_m value of CMC NFs (0.103 mM) was calculated (Fig. S8, ESI†). As depicted in Fig. 5D, the colorless TMB substrate can undergo gradual oxidation by H_2O_2 to form two colored oxidation products. In the initial stage, the FA–CMC NFs convert H_2O_2 to H_2O, rapidly forming blue charge-transfer diamine complexes with the radical cation in solution. These complexes exhibit intense absorption wavelengths at ~370 and ~652 nm, respectively. After adding H_2SO_4, the catalytic activity of FA–CMC NFs is inhibited, and the TMB molecule's cation radical loses another electron to form a diamine. The oxidized diamine product changes the blue solution to a yellow (yellow diamine) solution, with the more stable diamine product detected at an absorption wavelength of ~450 nm.[45] The results confirm that the CMC NFs possess peroxidase-like activity, and the TMB oxidation by NFs in the presence of H_2O_2 is illustrated in Fig. 5E. The abovementioned data indicate that the peroxidase-like activity of FA–CMC NFs can image cancer cells (MDA-MB-231 cells) in TMB and H_2O_2. Further study has demonstrated that the cancer cells are barely detectable in the presence of TMB and H_2O_2 (without NFs) (Fig. S9, ESI†). Moreover, blue-colored cancer cells were separated when MDA-MB-231 cells were incubated with FA–CMC NFs in the presence of TMB + H_2O_2. These findings suggest that FA–CMC NFs can function as a probe and accumulate on the surface or partially within cancer cells during imaging. The TMB molecules subsequently

adsorb on the surface of cancer cells due to electrostatic interaction between the negatively charged cell membrane and the positively charged TMB molecules. TMB on the cancer's surface is oxidized when H_2O_2 is added, generating a blue color. To detect cancer cells selectively using colorimetric methods, FA–CMC NFs were shown to possess intrinsic peroxidase activity, which is utilized for selective cancer cell detection. Notably, the functionalized FA on the CMC NF surface was adopted as a recognition component, which can efficiently trap tumor cells by attaching to overexpressing folate receptors and produce a colorimetric signal.[46] The folate receptor alpha (FR-α), a cell surface protein anchored to the cell, is upregulated in several types of epithelial cancer and 90% of ovarian cancers.[47,48] This protein is vital for folic acid (FA) transport within cells and is bound to FA-conjugated nanocarriers through receptor-mediated endocytosis.[49] Because FR-α is expressed at low levels in healthy tissues, it is an ideal target for delivering anticancer drugs specifically to tumors.[50] To achieve this, FA was attached to the surface of a nanocarrier made of FA-conjugated chitosan, which can bind to FR-α in most tumor cells,[51] enhancing accumulation at the tumor site.

Cancer cells that overexpress the folate receptor were chosen as the experimental cell line (MDA-MB-231 cells) in this assay. FA–CMC NFs serve as a colorimetric probe, selectively binding with the FA on the cancer cells' surface and generating a specific yellow color. The selectivity test was carried out using buffer (negative control) and human umbilical vein endothelial cells (HUVECs) (control cells), which did not show any color change after incubating TMB + H_2O_2 solution with FA–CMC NFs. The MDA-MB-231 cells showed a significant yellow color change. At the same time, they were incubated with TMB + H_2O_2 solution in the presence of FA–CMC NFs, and it could be revealed that FA–CMC NFs selectively target cancer cells compared to normal cells (HUVEC cells), as shown in Fig. 5F. For quantitative cancer cell detection, 40 μL of FA–CMC NFs (1 mg mL^{-1}) as a colorimetric probe were incubated with various concentrations of MDA-MB-231 cells from 50 to 55 000 in the presence of TMB and H_2O_2. The results showed that an increase in the concentration of cancer cells resulted in a corresponding increase in the absorbance of the oxTMB solution at 450 nm after adding H_2SO_4 solution, and the naked eye could also see the yellow color changes in the reaction (Fig. 5G). The yellow color in the reaction was due to the oxidation of the diamine under strongly acidic conditions (H_2SO_4), and the stable diamine product showed an utmost absorption wavelength of ~450 nm. The linear regression coefficient was observed to be 0.9937 for the target cells ranging from 50 cells per mL to 5.5×10^4 cells per mL (Fig. S10, ESI†). Hence, the FA–CMC NFs as a colorimetric probe to detect MDA-MB-231 cells has a lower limit of detection (LOD) of 10 cells per mL, higher than those in previously reported studies.[38,51] The yellow color generation was tested at different temperatures (10, 25, 37, and 50 °C) in the presence of MDA-MB-231 cells (5.5×10^4 cells per mL), as shown in Fig. S11 (ESI†). A relatively high catalytic activity was observed in the CMC NFs at 37 to 50 °C, with a relative activity of at least 90%, sufficiently catalyzing overexpressed H_2O_2 to kill cancer cells.

When the MDA-MB-231 cells were incubated with FA–CMC NFs for 24 h, the quantity of intracellularly adsorbed copper (Cu) and molybdenum (Mo) was measured through ICP-OES. The Cu and Mo ion concentration in untreated cells was 0.004 and 0.032 ppm, respectively. In contrast, the concentration of these ions in FA–CMC NF-treated cells was calculated to be 1.536 and 2.614 ppm, as shown in Fig. 6A. Heavy metal ions (Cu and Mo) are released from FA–CMC NFs due to the tumors' acidic environment. Previous research has shown that CuS nanoparticles can release copper ions (Cu^{2+}) in an acidic cancer environment, raising the cancer cell's ROS level.[52,53] In addition to their ability to detect cancer cells, the peroxidase activity of FA–CMC NFs can also treat cancer cells as they generate ·OH radicals efficiently. Methylene blue (MB) dye with its strong light absorption at 665 nm and the ability to generate free radicals makes it a popular choice in clinical applications against various diseases.[54,55] Its effectiveness against melanoma has been demonstrated in cell culture and it has been used to treat large melanoma lesions that are not eligible for surgery.[54] Furthermore, a previous study has indicated that MB is more toxic to leukemia cells than normal primary peripheral blood mononuclear cells (PBMCs),[56] indicating that it may be more effective in targeting cancer cells than normal cells. This is achieved by the MB dye molecules absorbing visible light and generating electrons on the surface of the FA–CMC NFs, which produces reactive oxygen species (ROS) that are highly effective in killing cancer cells. As shown in Fig. 6B, the MDA-MB-231 cells were treated with different concentrations (5–120 μg mL^{-1}) of FA–CMC NFs for 24 h, and their viability was determined using an MTT assay. The results showed the viability of MDA-MB-231 cells was calculated to be 96.5% even at a higher concentration of 120 μg mL^{-1}, indicating excellent biocompatibility of CMC NFs. The study also showed that the MDA-MB-231 cells had a higher cell death rate (73%) when treated with FA–CMC NF + MB and exposed to light (1 W LED) for 15 min, indicating enhanced therapeutic effects (Fig. S12, ESI†).

To evaluate the antitumor effects of FA–CMC NFs and MB, we carried out acridine orange (AO) and propidium iodide (PI) co-staining experiments. AO only fluoresces green in live cells, while PI only stains dead cells. Fig. 6C and S13 (ESI†) show that the MDA-MB-231 cells treated with control, bare FA–CMC NFs, MB, and FA–CMC NFs with MB without light showed almost no cell death. However, when we treated the MDA-MB-231 cells with FA–CMC NFs with MB and irradiated them with light, a large number of cells were stained red, indicating that the FA–CMC NFs with MB have enhanced therapeutic effects on MDA-MB-231 cells. One of the most widely used therapeutic strategies for cancer is oxidative stress, which is a mild therapy in cancer treatment. This therapy generates strong and excessive ROS, which damages cancer cells. However, due to their antioxidant defense capacity, normal cells can withstand a particular level of exogenous ROS stress.[57]

Fig. 6D illustrates the ROS-producing ability of different concentrations (5–100 μg mL^{-1}) of FA–CMC NFs with 10 μL MB (0.1 μg mL^{-1}) towards DCFH-DA stained MDA-MB-231 cells, following exposure to light. ROS can oxidize DCFH-DA to form DCF with bright fluorescence, which is detected by
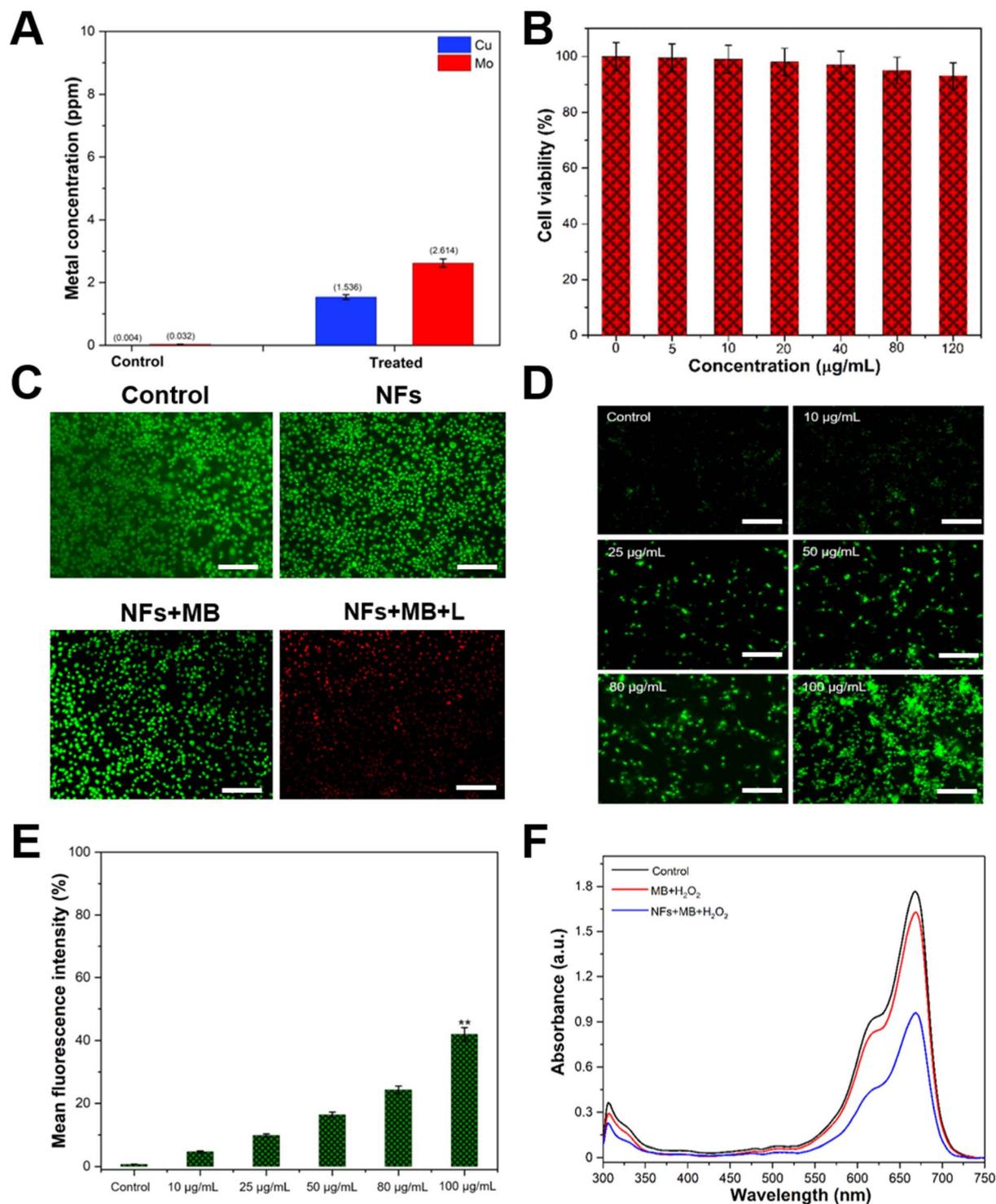
Fig. 6 (A) The adsorbed copper (Cu) and molybdenum (Mo) ions by MDA-MB-231 after incubation without and with CMC NFs for 24 h, quantified through the ICP-OES measurement and (B) the MDA-MB-231 cell viability after treatment with different concentrations (5–120 µg mL^{-1}) of CMC NFs for 24 h at 37 °C. (C) Fluorescence images of MDA-MB-231 cells stained with AO/PI after incubation with control, bare FA–CMC NFs and FA–CMC NFs with MB exposed to light (1 W LED) or not for 15 min, (D) *in vitro* ROS generation and (E) DCF fluorescence intensity of DCFH-DA stained MDA-MB-231 cells analyzed after being treated with various FA–CMC NF concentrations (5–100 µg mL^{-1}) + MB dye, exposed to light (1 W LED) for 15 min (scale bar 50 µm, 20× magnification), and (F) absorbance spectra of MB degradation (10 µL, 0.1 mg mL^{-1}) at 664 nm in the presence of FA–CMC NFs with 100 µL of H$_2$O$_2$ (5 mM), exposed to light (1 W LED) for 15 min.

a fluorescence spectrometer under an excitation of 488 nm. As the concentration of FA–CMC NFs increases, the fluorescence intensity of DCF also increases. The control group treated cells show minimal fluorescence, while the FA–CMC NFs with the MB treated group exhibit more robust green fluorescence. Fig. 6E displays the results of a fluorescence plate reader analysis of ROS intensity in cancer cells following treatment with various NF concentrations. The fluorescence intensity of MDA-MB-231 cells treated with 100 μg mL^{-1} of FA–CMC NFs combined with 10 μL of MB (0.1 μg mL^{-1}) was noticeably higher than that of other NF concentrations. Due to their peroxidase-like characteristics, the CMC NFs combined with MB have the potential to be effective candidates for cancer treatment, as increased ROS levels play a significant role in regulating cell death in cancer cells. The hydrophilic phenothiazine derivative of MB, with low redox potential, efficiently transports electrons in the mitochondrial membrane, reducing mitochondrial superoxide production. Additionally, MB can effectively enter biological compartments and generate singlet oxygen, destroying nucleic acid in a nuclease-like manner. As shown in Fig. 6F, the ability of different treatment groups, such as MB, MB + H$_2$O$_2$, and FA–CMC NF + MB + H$_2$O$_2$, to generate extracellular ˙OH was assessed with or without light conditions (1 W LED) for 15 min. The FA–CMC NF + MB + H$_2$O$_2$ group demonstrated efficient degradation of the MB dye and the solution color appeared to fade within 15 min, indicating the generation of ˙OH radicals. This finding revealed the FA–CMC NF + MB + H$_2$O$_2$ group's excellent capability to produce ˙OH free radicals in the presence of light, which can effectively kill cancer cells. The MoS$_2$/CuS nanostructures provide intact support to MB, facilitating a synergistic antioxidant response with extensive intracellular imaging potential. The results indicate that the nanostructures have superior capability to form ˙OH free radicals in the presence of light, which can effectively kill cancer cells with high efficiency.[27] In addition, ˙OH is generated by Fenton-like interactions between endogenous H$_2$O$_2$ of the tumor and Cu^{2+} ions produced in the tumor acidic environment from the FA–CMC NFs. Previous studies have also reported that the liberated Cu^{2+} can directly engage with H$_2$O$_2$ to produce ˙OH, leading to cancer cell demise through a Fenton-like mechanism. In contrast, the released copper can react with glutathione (GSH), reducing Cu^{2+} to Cu$^+$, which then unites with H$_2$O$_2$ to generate ˙OH radicals.[58] The mechanism most likely follows Fenton's reaction[59] and can be written as follows:

$$Cu^{2+} + H_2O_2 \rightarrow Cu^{1+} + HOO^{\cdot} + H^+$$

$$Cu^{1+} + H_2O_2 \rightarrow Cu^{2+} + {}^{\cdot}OH + OH^-$$

To determine the ˙OH generation capability of FA–CMC NFs, the conversion of H$_2$O$_2$ to ˙OH in the presence of FA–CMC NFs was determined. The detection of MB absorbance provided evidence of the formation of ˙OH from H$_2$O$_2$. Both the presence and the absence of H$_2$O$_2$ resulted in MB exhibiting a blue color and strong absorbance in an aqueous solution. The radical ion was produced through a Fenton-like reaction in the FA–CMC

NFs when interacted with MB and decolorized the solution. This led to a decrease in MB absorbance intensity. The absorbance dropped dramatically when FA–CMC NFs were added to the MB and H$_2$O$_2$ mixture. It was observed that the interaction between MB and ˙OH resulted in a decrease of the MB absorbance, suggesting that the FA–CMC NFs promoted the transformation of H$_2$O$_2$ to ˙OH. Furthermore, as the concentration of FA–CMC NFs increased, the absorbance of MB decreased accordingly.[58] The FA–CMC NFs can generate ˙OH radicals in the following way. When the FA–CMC NFs were irradiated with light energy, electron–hole pairs were developed by the excitation of electrons from the valence band to the conduction band.[60,61] These photogenerated holes were responsible for the production of more ˙OH radicals. This led to an increase in the ROS generation-based kill effect in the cancer cells.

3 Conclusion

In conclusion, we reported a novel 3D-CMC NF to develop a feasible and sensitive approach for detecting and treating cancer cells. A simple hydrothermal method was utilized to synthesize the CMC NF, exhibiting uniform flower-like structures with meso/microporosity, petal-like designs on the surface, and admirable dispersity. The interaction between FA-CMC NFs and TMB in the presence of H$_2$O$_2$ results in the formation of a blue-colored product. This is attributed to the formation of a blue charge-transfer diamine complex, which is supported by the prominent absorption peak observed at 652 nm. The results of this study indicate that the FA-CMC NFs possess peroxidase activity. After that, with the addition of H$_2$SO$_4$, the cation radical of the TMB molecule lost another electron to form a diamine, forming a yellow color product. The solution color change is both noticeable and easily observed by the naked eye. These characteristics of FA–CMC NFs were used as a colorimetric biosensor to detect MDA-MB-231 cells with a LOD of 10 cells per mL in a wide detection range (50 to 5.5 × 10^4 cells per mL). Besides their ability to detect cancer cells, the peroxidase activity of FA–CMC NFs was also capable of treating cancer cells because they generate ˙OH radicals efficiently. The FA–CMC NFs with MB + H$_2$O$_2$ showed an efficient degradation of the MB dye, and the solution color appeared to fade within 15 min, indicating that they generated ˙OH radicals. The finding revealed excellent capability to produce ˙OH free radicals, which can kill cancer cells. Hence, a high degree of specificity and robustness of the FA–CMC NFs is demonstrated by their ability to detect as well as treat cancer cells, which suggests that based on its simple peroxidase features, the FA–CMC NF could be an effective candidate for clinical cancer diagnosis and treatment.

4 Experimental section

4.1 Chemicals and materials

Calcium chloride (CaCl$_2$, 93.0%), 3-(4,5-dimethyl-2-thiazolyl)-2,5-diphenyltetrazolium bromide (MTT), sodium molybdate dihydrate (Na$_2$MoO$_4$·2H$_2$O, ≥99.5%), 3,3′,5,5′-tetramethylbenzidine (TMB, ≥98%), polyvinylpyrrolidone (PVP, M_w 40 000), 2′,7′-dichlorofluorescin diacetate (DCFH-DA, ≥95%),

thiourea (CH_4N_2S, ≥99%), hydrogen peroxide (H_2O_2), citric acid ($C_6H_8O_7$, ≥99.5%), acridine orange (AO, ≥98%), copper(II) nitrate hydrate ($Cu(NO_3)_2\cdot 2H_2O$, 99.9%), propidium iodide (PI, ≥95%), folic acid (≥97%), 1-ethyl-3-(3-dimethylaminopropyl) carbodiimide (EDC), dimethyl sulfoxide (DMSO), *N*-hydroxysuccinimide (NHS), (3-aminopropyl)triethoxysilane (3-APTES, ≥99%), 2,7-dichlorodihydrofluorescein diacetate (DCFH-DA, ≥97%), and sulfuric acid (H_2SO_4) were ordered from Sigma-Aldrich. All chemicals employed in the studies were of analytical reagent grade, and deionized water was utilized throughout the experiments.

4.2 Synthesis of CMC nanoflowers

The 3D CMC NF was synthesized by the hydrothermal method. Typically, 6 mM $CaCl_2$, 2.5 mM $Na_2MoO_4\cdot 2H_2O$, and 100 mg of PVP were added to 50 mL of distilled water and then, the mixture solution was sonicated for 10 min. Then, 13 mM CH_4N_2S was added dropwise to the reaction mixture and stirred magnetically for another 10 min. Afterward, the mixture solution containing 10 mM $C_6H_8O_7$ and 3 mM $Cu(NO_3)_2\cdot 2H_2O$ was added to the above reaction mixture and stirred for another 30 min. Subsequently, the reaction mixture was relocated to a stainless-steel autoclave lined with Teflon and positioned in an oven at 180 °C for 6 h. A black precipitate was collected by centrifugation after cooling the product to room temperature (RT) and washed three times with absolute ethanol and once with distilled water. Finally, CMC NFs were dried at 60 °C in a vacuum cabinet for further use.

4.3 Preparation of FA conjugated CMC NFs

To get FA conjugated NFs, firstly, 1 mL prepared CMC NF solution (1 mg mL^{-1}) was mixed with 50 μL of APTES and magnetically stirred for 6 h at RT. The unbounded APTES was separated by centrifugation and the pellet was resuspended in 1 mL Tris–PBS (pH 7.4); afterward, 1 mL of FA (0.2 mg mL^{-1}) solution containing NHS (1 mL, 0.5 mg mL^{-1}) and EDC (1 mL, 1 mg mL^{-1}) was added and mechanically stirred overnight.[38] The final product (FA–CMC NF) was separated by centrifugation and washed thrice with ultrapure water. Finally, the FA–CMC NFs were kept at 4 °C for further studies.

4.4 Characterization of CMC NFs

A high-resolution transmission electron microscope (HR-TEM, Hitachi/HF-3300) was utilized to determine the morphology and composition of NFs. The surface morphology and structure of CMC NFs were assessed using a high-resolution field-emission SEM (HR-FE-SEM, Hitachi/SU8020). Then, the absorption spectrum of FA–CMC NFs was acquired with a nanodrop (DS-11+, DeNovix, USA) spectrophotometer, in which the absorbance of the surface-modified NFs was studied as a function of wavelength. The X-ray diffraction (XRD, D/max-2550 PC XRD, Rigaku) technique was used to determine the crystallinity of CMC NFs at 2θ values of 10–80°. The purity and surface oxidation were demonstrated using an X-ray photoelectron spectrometer (XPS) in the fabricated CMC NFs (Thermo Scientific/ESCALAB 250Xi). The Raman spectrum of the nanoflower was

obtained using a inVia-Reflex micro-Raman spectroscopy (Thermo Scientific/Nicolet Almega XR) system using a laser with a wavelength of 532 nm.

4.5 Peroxidase-mimetic activity of CMC NFs

The peroxidase-mimetic activity of CMC NFs was studied by TMB catalytic oxidation in the presence of H_2O_2 at 37 °C. Briefly, 100 μL of H_2O_2 (10 mM), 10 μL of TMB (1 mM, DMSO solution), and 50 μL of CMC NF dispersion (1 mg mL^{-1}) were added into 0.2 M buffer solution (pH 4.0) with a make up to 1 mL volume. After a reaction time of 10 min, the TMB oxidation was accompanied by color changes, and the reaction solution was measured at 652 nm using UV-vis spectroscopy. The effects of pH, time, and temperature were investigated to optimize the catalytic conditions. In another experiment, H_2O_2 detection was assessed as follows; 100 μL of H_2O_2 with various concentrations (5–500 μM), 40 μL of CMC NF dispersion (1 mg mL^{-1}), and 10 μL of TMB (0.6 mM, DMSO solution) were added into buffer solution (pH 4) and incubated for 10 min at 37 °C. The reaction was performed in a 2 mL quartz cuvette; after the reaction for 10 min, the absorption spectra of the solution were analyzed in the wavelength range of 250–750 nm using a nanodrop spectrophotometer.

4.6 *In vitro* culture of human breast cancer (MDA-MB-231) cells

A CO_2 incubator was used to culture the MDA-MB-231 cells until they reached the cell confluency (80–85%). The cells were grown in a 25 cm^2 tissue culture plate supplied with 6 mL of DMEM medium consisting of 10% fetal bovine serum, 100 μg per mL streptomycin, and penicillin, and incubated at 37 °C under 90% humidity and 5% CO_2 gas, respectively. Finally, the MDA-MB-231 cells were rinsed thrice with PBS and gathered using 0.25% trypsin-ethylenediaminetetraacetic acid (EDTA) for further studies.

4.7 Cancer cell imaging and the element content analysis by ICP measurement

Each well of the 96-well plate was seeded with 3×10^1 cells and the cells were incubated using a CO_2 incubator supplied with 90% humidity and 5% CO_2 gas at 37 °C to reach a cell confluency of up to 80–85%. After 24 h incubation, the MDA-MB-231 and HUVEC cells were washed twice with PBS, 40 μL of FA–CMC NFs (1 mg mL^{-1}, DMEM medium) was added, and incubated for 4 h. Then, 50 μL of H_2O_2 (5 mM) and 10 μL of TMB (0.5 mM) were supplied to each well and incubated for another 10 min. Afterwards, the cells were washed with PBS to remove the unattached FA–CMC NF, excessive H_2O_2, and TMB. Then, the colored cells were observed using microscopy (LSM700, Zeiss, Germany).

To determine the adsorbed metal ion, the MDA-MB-231 cells were gently washed and digested with strong nitric acid after 4 h incubation with FA–CMC NFs. Then, the copper and molybdenum contents were assessed by inductively coupled plasma mass spectrometry (ICP-MS) to examine the physical adsorption of endocytosed NFs.

4.8 Colorimetric detection of MDA-MB-231 cells

Human MDA-MB-231 cells at a concentration of approximately 5×10^1 to 5.5×10^4 cells per mL were grown for 24 h at 37 °C using a 96-well plate for the colorimetric detection of cancer cells. Then, the cells were washed twice with 0.2 M PBS (pH 7.4), and 4% formaldehyde solution was used to fix the cells for 10 min. Then, the excess formaldehyde was removed by PBS washing and incubating with 50 μL FA–CMC NFs for 2 h. Afterwards, each well with cells was washed thrice with fresh PBS (pH = 7.4) to remove unattached FA–CMC NFs. Thereupon, 200 μL of PBS (0.1 M, pH = 5.5) consisting of 0.6 mM TMB and 5 mM H_2O_2 was supplied to each well and incubated for 10 min. Then, 0.3 M H_2SO_4 was added to every well to terminate the reaction, and quantitative measurement was performed for the color (yellow) reaction.

To evaluate the temperature effect on the colorimetric detection of cancer cells, the MDA-MB-231 cells (5.5×10^4 cells per mL) were grown for 24 h. Thereupon, 200 μL of PBS (0.1 M, pH = 5.5) consisting of 0.6 mM TMB and 5 mM H_2O_2 was supplied to each well and incubated for 10 min at different temperatures such as 10, 25, 37, and 50 °C. Then, 0.3 M H_2SO_4 was added to every well to terminate the reaction, and quantitative measurement was performed for the color (yellow) reaction.

4.9 Cancer therapy of FA–CMC NFs with methylene blue (MB)

The MDA-MB-231 cell viability towards CMC NFs was determined by using the cells at a density of 4×10^2 cells per well and the cell confluency was allowed to reach up to 80–85% in a 96-well plate. Afterwards, different concentrations (5–120 μg mL^{-1}) of CMC NFs were incubated with MDA-MB-231 cells for 20 h. After that, each well was supplied with 100 μL of MTT (5 mg mL^{-1}) solution and incubated for another 4 h. Finally, the formed formazan crystal was diluted using 200 μL of DMSO and the intensity at 570 nm was observed using a microplate reader.

To examine the therapeutic efficacy of NFs with MB, the MDA-MB-231 cells (4×10^2 cells per well) were seeded in a 96-well plate; after reaching the cell confluency, the cells were then treated with saline (control) and incubated with 40 μL of FA–CMC NFs (1 mg mL^{-1}) for 20 h at 37 °C. For therapeutic purposes, the MDA-MB-231 cells were thoroughly washed with PBS and incubated with 10 μL MB (0.1 μg mL^{-1}) for 4 h. The cells in the culture plate were either exposed or not exposed to a 1 W LED lamp for 15 min, followed by an incubation period of 24 h. Finally, the absorbance intensity of each well with MDA-MB-231 cell was measured at 570 nm using a microplate reader to determine the cell viability.

4.10 *In vitro* antitumor effect

To investigate the anti-tumor effects of NFs, experimental MDA-MB-231 cells (4×10^2 cells per well) were seeded in a 96-well plate for 12 h; after reaching the cell confluency, the cells were then treated with saline (control) and 40 μL of FA–CMC NFs (1

mg mL^{-1}) incubated for another 12 h. For the therapeutic purpose, the MDA-MB-231 cells were then thoroughly rinsed with PBS and incubated with 10 μL MB (0.1 μg mL^{-1}) for another 4 h. Afterwards, the cells were immediately exposed or not exposed to a 1 W LED lamp for 15 min and incubated for another 24 h. Moreover, the treated MDA-MB-231 cells were rinsed thrice with PBS, stained with 10 μL of PI (3 mg mL^{-1}) and AO (3 mg mL^{-1}) for 20 min, and then using an inverted fluorescence microscope (LSM700, Zeiss, Germany), the stained cells were observed.

4.11 Reactive oxygen species (ROS) generation assay

The level of ROS in treated cancer cells was measured using DCFDA staining, which is a method that detects intracellular ROS generation. It depends upon converting the fluorescence dye DCFH-DA to 2′,7′-dichlorofluorescein (DCF). The DCFH-DA dye possesses the ability to permeate cancer cells, and after that, DCFH-DA is converted into DCFH due to removal of acetyl groups by esterase enzyme inside the cancer cell. Then, the DCFH is oxidized and converted into green fluorescence-producing DCF by the activity of intracellular ROS small molecules. To quantify the intracellular ROS level, experimental MDA-MB-231 cells (4×10^2 cells per well) were seeded in a 96-well plate for 12 h at 37 °C; after reaching the cell confluency, the cells were then treated with saline (control), and incubated with 40 μL of FA–CMC NFs (1 mg mL^{-1}) for 12 h. Then, the MDA-MB-231 cells were carefully washed with PBS and incubated with 10 μL MB (0.1 μg mL^{-1}) for another 4 h. Afterwards, the cells were immediately exposed or not exposed to a 1 W LED lamp for 15 min and incubated for another 24 h. Then, the treated MDA-MB-231 cells were stained with 20 μL of DCFH-DA (1 mg mL^{-1}) for 20 min and rinsed twice with fresh PBS and the cells were observed using an inverted fluorescence (LSM700, Zeiss, Germany) microscope to quantify the intracellular green fluorescence of DCF at an excitation wavelength and an emission wavelength (485 nm and 530 nm), respectively.

4.12 Methylene blue (MB) degradation test

The effects of FA–CMC NFs in the formation of ˙OH species was verified using nanoflowers and MB in the presence of 5 mM H_2O_2. Briefly, 1 mL of buffer solutions (pH 4) containing 5 mM H_2O_2 was mixed with 10 μL of MB solution (0.1 mg mL^{-1}). Then, the mixture solution was gently shaken for 15 min at 37 °C under light conditions (1 W LED), followed by the addition of 40 μL of FA–CMC NFs (1 mg mL^{-1}). Afterwards, the CMC NFs were collected at 10 000 rpm for 10 min by centrifugation and the amount of MB was quantitatively estimated in the supernatant at 664 nm. The generation of ˙OH species is directly proportional to the decrease in the MB absorbance peak at 664 nm.

Author contributions

Chandran Murugan: conceptualization, data curation, writing-original draft, validation, and methodology. Hyoryong Lee

conducted data analysis and co-revised the manuscript. Sukho Park: funding acquisition, writing-review & editing, and supervision.

Conflicts of interest

There are no conflicts to declare.

Acknowledgements

References

1 N. M. Phan, T. L. Nguyen and J. Kim, Nanozyme-based enhanced cancer immunotherapy, *Tissue Eng. Regener. Med.*, 2022, **19**, 237–252.

2 C. Murugan and S. Park, Cerium ferrite@ molybdenum disulfide nanozyme for intracellular ROS generation and photothermal-based cancer therapy, *J. Photochem. Photobiol., A*, 2023, **437**, 114466.

3 R. Zhang, X. Yan and K. Fan, Nanozymes inspired by natural enzymes, *Acc. Mater. Res.*, 2021, **2**, 534–547.

4 C. Hong, X. Meng, J. He, K. Fan and X. Yan, Nanozyme: A promising tool from clinical diagnosis and environmental monitoring to wastewater treatment, *Particuology*, 2022, **71**, 90–107.

5 H. Wei, *et al.*, Nanozymes: A clear definition with fuzzy edges, *Nano Today*, 2021, **40**, 1016.

6 C. Murugan, N. Murugan, A. K. Sundramoorthy and A. Sundaramurthy, Nanoceria decorated flower-like molybdenum sulphide nanoflakes: an efficient nanozyme for tumour selective ROS generation and photo thermal therapy, *Chem. Commun.*, 2019, **55**, 8017–8020.

7 F. Arshad, N. F. Mohd-Naim, R. Chandrawati, D. Cozzolino and M. U. Ahmed, Nanozyme-based sensors for detection of food biomarkers: a review, *RSC Adv.*, 2022, **12**, 26160–26175.

8 H. Wang, K. Wan and X. Shi, Recent advances in nanozyme research, *Adv. Mater.*, 2019, **31**, 1805368.

9 F. Canonica, *et al.*, Structural basis and mechanism for metallochaperone-assisted assembly of the CuA center in cytochrome oxidase, *Sci. Adv.*, 2019, **5**(7), eaaw8478.

10 K. S. Muthuvelu, R. Rajarathinam, R. N. Selvaraj and V. B. Rajendren, A novel method for improving laccase activity by immobilization onto copper ferrite nanoparticles for lignin degradation, *Int. J. Biol. Macromol.*, 2020, **152**, 1098–1107.

11 T. Soltani and B.-K. Lee, Enhanced formation of sulfate radicals by metal-doped BiFeO3 under visible light for improving photo-Fenton catalytic degradation of 2-chlorophenol, *Chem. Eng. J.*, 2017, **313**, 1258–1268.

12 B. Ma, *et al.*, Self-assembled copper–amino acid nanoparticles for in situ glutathione "AND" H2O2 sequentially triggered chemodynamic therapy, *J. Am. Chem. Soc.*, 2018, **141**, 849–857.

13 Z. Chen, *et al.*, Acute toxicological effects of copper nanoparticles in vivo, *Toxicol. Lett.*, 2006, **163**, 109–120.

14 R. Lei, *et al.*, Integrated metabolomic analysis of the nano-sized copper particle-induced hepatotoxicity and nephrotoxicity in rats: a rapid in vivo screening method for nanotoxicity, *Toxicol. Appl. Pharmacol.*, 2008, **232**, 292–301.

15 R. J. Griffitt, *et al.*, Exposure to copper nanoparticles causes gill injury and acute lethality in zebrafish (Danio rerio), *Environ. Sci. Technol.*, 2007, **41**, 8178–8186.

16 A. Pandey, *et al.*, Photon and electron beam pumped luminescence of Ho3+ activated CaMoO4 phosphor, *Appl. Surf. Sci.*, 2017, **423**, 1169–1175.

17 Y. Xie, *et al.*, Controlled synthesis and luminescence properties of CaMoO4: Eu3+ microcrystals, *Opt. Mater.*, 2018, **77**, 13–18.

18 Y. Zhai, *et al.*, CaMoO4: Dy3+, Eu3+ phosphors: microwave synthesis, characterization, tunable luminescence properties and energy transfer mechanism, *Optik*, 2018, **164**, 433–442.

19 A. Parchur, *et al.*, Enhanced luminescence of CaMoO4: Eu by core@ shell formation and its hyperthermia study after hybrid formation with Fe3O4: cytotoxicity assessment on human liver cancer cells and mesenchymal stem cells, *Integr. Biol.*, 2014, **6**, 53–64.

20 S. K. Shinde, *et al.*, Synthesis of 3D nanoflower-like mesoporous NiCo2O4 N-doped CNTs nanocomposite for solid-state hybrid supercapacitor; efficient material for the positive electrode, *Ceram. Int.*, 2021, **47**, 31650–31665.

21 I. G. Subramani, *et al.*, 3D nanoporous hybrid nanoflower for enhanced non-faradaic redox-free electrochemical impedimetric biodetermination, *J. Taiwan Inst. Chem. Eng.*, 2020, **116**, 26–35.

22 S. Adhikari, D. Sarkar and G. Madras, Hierarchical design of CuS architectures for visible light photocatalysis of 4-chlorophenol, *ACS Omega*, 2017, **2**, 4009–4021.

23 A. Mondal, A. Paul, D. N. Srivastava and A. B. Panda, Defect- and phase-induced acceleration of electrocatalytic hydrogen production by ultrathin and small MoS2-decorated rGO sheets, *ACS Appl. Nano Mater.*, 2018, **1**, 4622–4632.

24 V. M. Longo, *et al.*, Hierarchical assembly of CaMoO4 nano-octahedrons and their photoluminescence properties, *J. Phys. Chem. C*, 2011, **115**, 5207–5219.

25 M. M. Muhsen, S. M. Al-Jawad and A. A. Taha, Gum Arabic-modified Mn-doped CuS nanoprisms for cancer photothermal treatment, *Chem. Pap.*, 2022, **76**, 6821–6838.

26 J. Miao, *et al.*, Hierarchical Ni-Mo-S nanosheets on carbon fiber cloth: A flexible electrode for efficient hydrogen generation in neutral electrolyte, *Sci. Adv.*, 2015, **1**, e1500259.

27 S. Ramamoorthy, S. Bajhal and A. Sundaramurthy, The role of surface modification in improving the effectiveness of CuS nanorods for cancer ablation therapy and antibacterial applications, *Surf. Interfaces*, 2023, **39**, 103001.

28 R. Rajaram, *et al.*, Amperometric determination of Myo-inositol using a glassy carbon electrode modified with nanostructured copper sulfide, *Microchim. Acta*, 2020, **187**, 1–9.

29 M. Abdelfatah, et al., Effect of potentiostatic and galvanostatic electrodeposition modes on the basic parameters of solar cells based on Cu2O thin films, ECS J. Solid State Sci. Technol., 2016, 5, Q183.

30 A. C. Estrada, F. M. Silva, S. F. Soares, J. A. Coutinho and T. Trindade, An ionic liquid route to prepare copper sulphide nanocrystals aiming at photocatalytic applications, RSC Adv., 2016, 6, 34521–34528.

31 H. Yu, et al., Three-dimensional hierarchical architectures constructed by graphene/MoS2 nanoflake arrays and their rapid charging/discharging properties as lithium-ion battery anodes, Chem.–Eur. J., 2013, 19, 5818–5823.

32 H. Cheng, et al., Calcium glycerolate catalyst derived from eggshell waste for cyclopentadecanolide synthesis, Front. Chem., 2021, 9, 770247.

33 L. Cui, J. Wu, J. Li and H. Ju, Electrochemical sensor for lead cation sensitized with a DNA functionalized porphyrinic metal–organic framework, Anal. Chem., 2015, 87, 10635–10641.

34 H. Sun, et al., Electronic coupling between molybdenum disulfide and gold nanoparticles to enhance the peroxidase activity for the colorimetric immunoassays of hydrogen peroxide and cancer cells, J. Colloid Interface Sci., 2020, 578, 366–378.

35 X. Ji, et al., Dual-active Au@ PNIPAm nanozymes for glucose detection and intracellular H2O2 modulation, Langmuir, 2022, 38, 8077–8086.

36 A. Mehdinia, S. Heydari and A. Jabbari, Synthesis and characterization of reduced graphene oxide-Fe3O4@ polydopamine and application for adsorption of lead ions: Isotherm and kinetic studies, Mater. Chem. Phys., 2020, 239, 121964.

37 W. Lu, S. Chen, H. Zhang, J. Qiu and X. Liu, FeNC single atom nanozymes with dual enzyme-mimicking activities for colorimetric detection of hydrogen peroxide and glutathione, Journal of Materiomics, 2022, 8, 1251–1259.

38 N. Alizadeh, et al., Hierarchical Co (OH) 2/FeOOH/WO3 ternary nanoflowers as a dual-function enzyme with pH-switchable peroxidase and catalase mimic activities for cancer cell detection and enhanced photodynamic therapy, Chem. Eng. J., 2021, 417, 129134.

39 L. Gao, et al. Intrinsic peroxidase-like activity of ferromagnetic nanoparticles, Nat. Nanotechnol., 2007, 2, 577–583.

40 Q. Jia, et al., Synergistic catalysis of Au–Cu/TiO 2-NB nanopaper in aerobic oxidation of benzyl alcohol, J. Mater. Chem. A, 2014, 2, 16292–16298.

41 W. He, et al., Understanding the formation of CuS concave superstructures with peroxidase-like activity, Nanoscale, 2012, 4, 3501–3506.

42 J. Huang, et al., MoS2 nanosheet functionalized with Cu nanoparticles and its application for glucose detection, Mater. Res. Bull., 2013, 48, 4544–4547.

43 C. Song, et al., High peroxidase-like activity realized by facile synthesis of FeS2 nanoparticles for sensitive colorimetric detection of H2O2 and glutathione, Biosens. Bioelectron., 2020, 151, 111983.

44 Y. Tao, Y. Lin, Z. Huang, J. Ren and X. Qu, Incorporating graphene oxide and gold nanoclusters: a synergistic catalyst with surprisingly high peroxidase-like activity over a broad pH range and its application for cancer cell detection, Adv. Mater., 2013, 25, 2594–2599.

45 G.-L. Wang, et al., Dual responsive enzyme mimicking activity of AgX (X= Cl, Br, I) nanoparticles and its application for cancer cell detection, ACS Appl. Mater. Interfaces, 2014, 6, 6434–6442.

46 N. Patel, L. Ghali, I. Roitt, L. P. Munoz and R. Bayford, Exploiting the efficacy of Tyro3 and folate receptors to enhance the delivery of gold nanoparticles into colorectal cancer cells in vitro, Nanoscale Adv., 2021, 3, 5373–5386.

47 A. Cheung, et al., Targeting folate receptor alpha for cancer treatment, Oncotarget, 2016, 7, 52553.

48 A. Kurosaki, et al., Serum folate receptor alpha as a biomarker for ovarian cancer: Implications for diagnosis, prognosis and predicting its local tumor expression, Int. J. Cancer, 2016, 138, 1994–2002.

49 Z. Hou, et al., Dual targeting of epithelial ovarian cancer via folate receptor α and the proton-coupled folate transporter with 6-substituted pyrrolo [2, 3-d] pyrimidine antifolates, Mol. Cancer Ther., 2017, 16, 819–830.

50 D. Paolino, et al., Folate-targeted supramolecular vesicular aggregates as a new frontier for effective anticancer treatment in in vivo model, Eur. J. Pharm. Biopharm., 2012, 82, 94–102.

51 Y. Song, Y. Chen, L. Feng, J. Ren and X. Qu, Selective and quantitative cancer cell detection using target-directed functionalized graphene and its synergetic peroxidase-like activity, Chem. Commun., 2011, 47, 4436–4438.

52 Q. Pan, et al., In-situ drug generation and controllable loading: rational design of copper-based nanosystems for chemo-photothermal cancer therapy, Chem. Eng. J., 2021, 409, 128222.

53 H.-X. Tang, et al., Biodegradable quantum composites for synergistic photothermal therapy and copper-enhanced chemotherapy, ACS Appl. Mater. Interfaces, 2020, 12, 47289–47298.

54 M. Wagner, et al., Methylene blue photodynamic therapy in malignant melanoma decreases expression of proliferating cell nuclear antigen and heparanases, Clin. Exp. Dermatol., 2012, 37, 527–533.

55 S. K. Bisland, C. Chien, B. C. Wilson and S. Burch, Pre-clinical in vitro and in vivo studies to examine the potential use of photodynamic therapy in the treatment of osteomyelitis, Photochem. Photobiol. Sci., 2006, 5, 31–38.

56 C. Kirszberg, V. Rumjanek and M. Capella, Methylene blue is more toxic to erythroleukemic cells than to normal peripheral blood mononuclear cells: a possible use in chemotherapy, Cancer Chemother. Pharmacol., 2005, 56, 659–665.

57 Y. Wang, et al., The double-edged roles of ROS in cancer prevention and therapy, Theranostics, 2021, 11, 4839.

58 M. Amereh, et al., ROS induction within 4T1 breast cancer cells by CuS NPs as chemodynamic agent, J. Drug Delivery Sci. Technol., 2023, 104689.

59 W. P. Kwan and B. M. Voelker, Rates of hydroxyl radical generation and organic compound oxidation in mineral-

catalyzed Fenton-like systems, *Environ. Sci. Technol.*, 2003, **37**, 1150–1158.

60 M. Behnajady, N. Modirshahla and R. Hamzavi, Kinetic study on photocatalytic degradation of CI Acid Yellow 23 by ZnO photocatalyst, *J. Hazard. Mater.*, 2006, **133**, 226–232.

61 E. Evgenidou, K. Fytianos and I. Poulios, Semiconductor-sensitized photodegradation of dichlorvos in water using TiO_2 and ZnO as catalysts, *Appl. Catal., B*, 2005, **59**, 81–89.